Feasibility studies for filament detection in resistively switching SrTiO3 devices by employing grazing incidence small angle X-ray scattering

S. Stille, C. Baeumer, S. Krannich, C. Lenser, R. Dittmann et al.

Additional information on J. Appl. Phys.

Feasibility studies for filament detection in resistively switching SrTiO$_3$ devices by employing grazing incidence small angle X-ray scattering

S. Stille,[1,a] C. Baeumer,[1] S. Krannich,[1] C. Lenser,[2] R. Dittmann,[2] J. Perlich,[3] S. V. Roth,[3] R. Waser,[2,4] and U. Klemradt[1,b]

[1]II. Institute of Physics and JARA-FIT, RWTH Aachen University, D-52056 Aachen, Germany
[2]Peter Gruenberg Institute and JARA-FIT, FZ Juelich, D-52425 Juelich, Germany
[3]HASYLAB, DESY, D-22607 Hamburg, Germany
[4]Institute of Materials in Electrical Engineering and Information Technology II, RWTH Aachen University, D-52056 Aachen, Germany

We report on fundamental studies of grazing incidence small angle X-ray scattering (GISAXS) on resistively switching SrTiO$_3$ thin film metal-insulator-metal (MIM) devices. Different influence factors on the GISAXS scattering pattern, e.g., surface morphology and top electrode material, were evaluated by simulations and compared with subsequent measurements. Pt top electrodes cause a strong background scattering which covers any information from the underlying SrTiO$_3$ layer. In order to reduce this undesired background scattering, the lighter elements Al and Ti have been used. In case of Ti top electrodes, we observed that a laterally formed structure occurs in the SrTiO$_3$ prior to any electrical treatment, which is consistent with the forming-free properties of the MIM structures. For Al top electrodes, we could detect a significant influence of an electroforming step on the scattered intensity. © 2013 American Institute of Physics. [http://dx.doi.org/10.1063/1.4792035]

I. INTRODUCTION

Resistance random access memory, short RRAM, which employs two or more resistive states of a material for data storage, has attracted considerable attention as a highly scalable future non-volatile memory concept.[1,2] A large variety of binary and ternary oxides exhibit resistive switching phenomena; however, the details of the complex microscopic mechanisms are rarely understood. In the search for promising oxide materials for future non-volatile memories, special attention has to be paid to their scaling capabilities.

The issue of scaling is strongly linked to the question whether the switching current is distributed homogeneously across the device area or localized to one or a few conducting filaments. While in the former case, the scaling limit will be connected to the minimum device area that guarantees sufficient switching currents for a reliable circuit operation; in the latter case, scaling might suffer from too large filament dimensions or their insufficient density and regularity within the material.

Therefore, the details of the filament formation, e.g., their size and distribution, in a specific device configuration are of key importance in order to assess the ultimate scaling limits for future RRAM devices. The spatial distribution of the current in RRAM devices has been to some extent studied by surface sensitive methods, e.g., conductive tip atomic force microscopy[3–5] or spectromicroscopy;[4–7] however, these methods only provide information about the exits of filaments at the device surface or interface. Transmission electron microscopy (TEM) or Transmission electron spectroscopy has been successfully employed to detect filament formation in resistive switching devices.[8,9] Besides its destructive nature, TEM is hampered by the very local information which prevents the collection of representative information on statistically distributed elements like filaments in a resistively switching device.

Grazing incidence small angle X-ray scattering (GISAXS) in principle provides information about nanoscale statistically distributed buried structures as far as a sufficient contrast in the electron density is provided. GISAXS experiments have first been carried out in 1989 by Levine et al. to characterize thin film growth.[10] Since then they have been applied to a variety of samples in nano-science and nano-technology.[11] Structures of the size of a few up to several hundred nanometer can be resolved, depending on the setup. GISAXS measurements are non-destructive and sensitive to thin films and their interfaces. This makes them a suitable technique to study structural properties of thin layers inside MIM devices.

The model system SrTiO$_3$ is considered in this work. The focus lies on different influence factors on the scattered intensity. Different top electrodes are used since they lead to different electrical forming behavior of the memory cells and differ in their influence on X-ray experiments. Whereas for Pt a high attenuation of the beam is expected, Al and Ti are much more X-ray transparent, offering a significantly improved information depth for the measurements.[12] Furthermore, undesired background scattering is expected to be much lower for Al and Ti than for Pt electrodes. In this work, the undesired scattering from parts of the devices (e.g., the electrodes), which are not in the focus of the GISAXS experiments, is referred to as "background scattering" due to its rather featureless character. It dominates significantly over other background contributions (air scattering, Compton scattering, etc.).

[a]sebastian.stille@rwth-aachen.de.
[b]klemradt@physik.rwth-aachen.de.

II. EXPERIMENTAL DETAILS

A. Samples preparation

We investigated single crystalline thin films of the resistive switching model material $SrTiO_3$ (STO) with intentional Fe acceptor doping in order to prevent the influence of unintended background impurity acceptor doping. Thin films of $20\,nm$ $SrTi_{1-x}Fe_xO_3$ (Fe:STO) with $x = 0.01$ were grown epitaxially on commercially available, (001) oriented, 1 at.% Nb-doped $SrTiO_3$ (Nb:STO) single crystals by pulsed laser deposition (PLD), using a KrF excimer-laser ($\lambda = 248$ nm) with an energy density of $0.8\,J/cm^2$, a frequency of 5 Hz, and a substrate temperature of $700\,°C$ at an oxygen pressure of 0.25 mbars (for more details, see Refs. [13] and [14]). For the top electrodes, Pt and Ti were deposited by sputtering and subsequently patterned by optical lithography. Al was deposited by electron beam evaporation. Top electrodes consisting of Pt only were also deposited by electron beam evaporation. A sketch of the stacking sequence of the samples is shown in Fig. 1(a).

Fig. 1(b) presents a bird's eye view of our samples. Each of them contained arrays with electrodes of different size ($20 \times 20\,\mu m^2$, $50 \times 50\,\mu m^2$, $100 \times 100\,\mu m^2$) and a distance of $5\,\mu m$ between the electrodes. Experiments on arrays instead of single cells have been necessary in order to account for the footprint of the X-ray beam which is around several millimeters. To study the influence of electrical treatments, each array existed twice in order to compare the measured GISAXS intensity with a reference value from as-deposited memory cells. In between the electrode arrays, Cu structures were placed for alignment of the X-ray beam. An overview of the samples used for GISAXS measurements can be found in Table I.

B. Electrical properties

Electrical measurements have been carried out with an *Agilent B1500A* system. In all samples I-IV, stable resistive switching was observed. Depending on the sample system, the respective *I-V*-curves differ from each other. The necessity of a forming step during the first cycle depends on the sample system as can be seen in Fig. 2.

Samples with Pt top electrodes show resistive switching in eightwise polarity[14] with respect to the top electrode (cf. Fig. 2(a)). The first *I-V* cy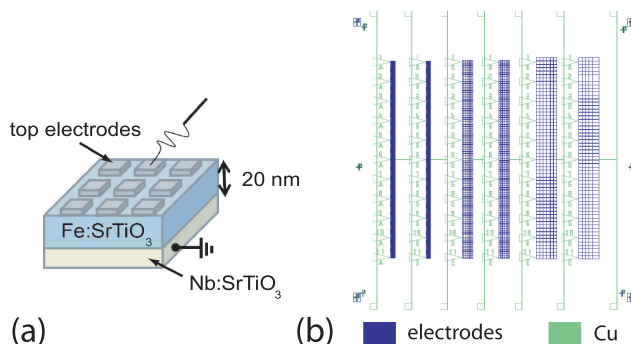cle (indicated in red) differs from the following ones. By applying a positive voltage, the resistance of the stack is reduced significantly, which is connected to an irreversible forming step. The sample is then in the low resistive ON state and can be switched stably.

Samples with Ti top electrodes above a critical thickness between 5 and 10 nm are likely to be forming-free due to a reduced initial resistance of the as-deposited samples.[15] Fig. 2(b) shows an example for a forming free device. For details on this sample system and the dependence of the initial resistance on the electrode thickness, please refer to Ref. [15].

For Al electrodes, switching in both eightwise and counter eightwise polarity[14] was observed. In the former case (cf. Fig. 2(c)), the first *I-V* sweep differs only slightly from the following ones (indicated in red). In the latter case (cf. Fig. 2(d)), the resistance of the sample drops significantly during the first cycle (red line). This behavior is connected to an irreversible forming step here as in the case of the Pt top electrodes. Afterwards, the sample is switching stably in counter-eightwise polarity.

In the case of eight-wise switching, for all samples, a nonlinear transport process was observed for positive and
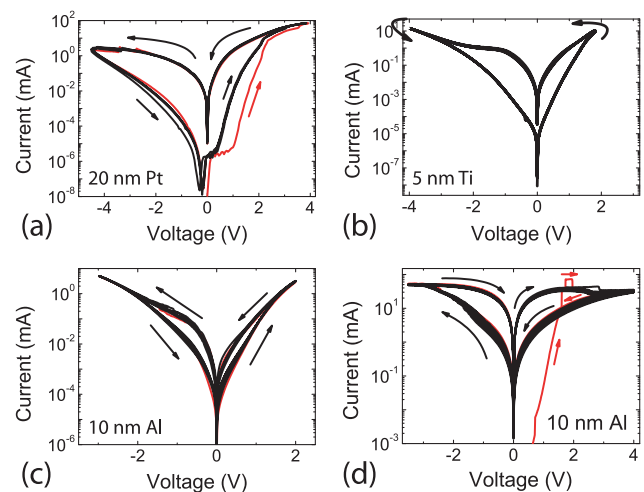
TABLE I. Overview of top electrodes for samples prepared for GISAXS experiments. The samples in general consisted of top electrodes/20 nm Fe:STO/ Nb:STO.

Sample	Top electrodes
I	20 nm Pt
II	5 nm Ti
III	15 nm Ti
IV	10 nm Al

FIG. 2. *I-V* curves demonstrating the forming behavior of the different sample systems. The first cycle is drawn in red. (a) Samples with Pt top electrodes show an irreversible forming step during the first cycle. Afterwards, stable resistive switching in eightwise polarity is observed. (b) The forming behavior of samples with Ti top electrodes depends strongly on the initial resistance which is depending on the electrode thickness.[15] This example shows a forming free electrode with a Ti thickness of 5 nm. (c) At low voltages, samples with Al top electrodes show resistive switching in eightwise polarity. The first cycle differs only slightly from the following ones. (d) If one increases the voltage, the flowing current increases suddenly. This is connected to an irreversible forming step. After this change of the sample, resistive switching in counter-eightwise polarity takes place.

FIG. 1. (a) Sketch of the samples geometry.[15] (b) Top view on the structured pattern for GISAXS measurements.

negative voltages that can be fitted to a thermionic emission through a Schottky barrier. The transport in the high resistive OFF state in counter eightwise polarity switching of sample IV (10 nm Al) can be described by a Poole-Frenkel emission.

To prepare the samples for GISAXS experiment, one array of each electrode size has been exposed to a positive voltage sweep until a significant drop in resistance was observed. The applied voltage differed from sample to sample but has always been below 5 V. For the electrical characterization, the top electrodes made of Ti and Al have been capped by a 5 nm thick Pt layer to prevent the samples from oxidation and in order to facilitate the measurements. For the GISAXS experiments, no capping layer was used to increase the information depth of the X-ray beam. The thickness of Ti for the GISAXS samples has been chosen in order to cover both high and low initial resistance (cf. Ref. 15). For Al (sample IV), the thickness of the top electrodes does not have this influence. The system with 10 nm thick top electrodes has been found to be the most reliable in our pretests.

C. GISAXS measurements

GISAXS measurements have been performed at beamlines BW4 (Ref. 16) and P03 (Ref. 17) (DESY, Hamburg) at wavelengths of $\lambda = 1.383 \cdot 10^{-10}$ m ($E_\gamma = 8.98$ keV) and $\lambda = 0.976 \cdot 10^{-10}$ m ($E_\gamma = 12.70$ keV), respectively. At BW4, the distance between sample and the detector (*marCCD 165*) was 2.3 m, covering a Δq-range from 7×10^{-3} to 1.6 nm^{-1}. At P03, a *Pilatus 300k* detector was used at a distance of 4.5 m from the sample. This covered a Δq-range from 5×10^{-3} to 1.0 nm^{-1}. This way, structures of size from around 10 to a few 100 nm could be resolved. An angle of incidence of $\alpha_i = 0.7°$ has been used in order to optimize the penetration depth of the X-ray beam for our samples. Due to the large

projection of the X-ray beam onto the sample, being only slightly smaller than the size of the sample (10 mm), an orientation of the electrode arrays along the X-ray beam was essential for the GISAXS experiments (cf. Fig. 1(b) and Fig. 3). This has been realized by the already mentioned Cu structures. When Cu is exposed to the X-ray beam, the emitted fluorescence radiation can be analyzed in order to ensure a proper alignment of the sample. This has been done by observing the K$_\alpha$-line of Cu at 8 keV with a *Vortex EM SII* silicon drift detector.

III. SIMULATIONS OF GISAXS INTENSITIES

Prior to the experiments, we performed simulations in order to estimate the influence of the top electrode material, the surface roughness, and the filament structure on the GISAXS pattern. Simulations of GISAXS intensities have been carried out using the software FitGISAXS.[18] The indices of refraction of the materials in the form $n = 1 - \delta - i\beta$ have been calculated using the *CXRO* database.[12] For the calculations, a wavelength of $\lambda = 1.383 \times 10^{-10}$ m has been used. The angle of incidence has been fixed at $0.7°$.

Searching for lateral dimensions of the scatterers, we put the focus of the simulations and later data treatment on lateral cuts in the scattering pattern. The intensity along this direction is given by

$$I(q_y) \propto |F(q_y)|^2 S(q_y), \tag{1}$$

with F being the form factor of individual scatterers and S the interference function related to their spacial distribution. For the size of the scatterers, the local monodisperse approximation[11] and a log-normal size distribution have been used.
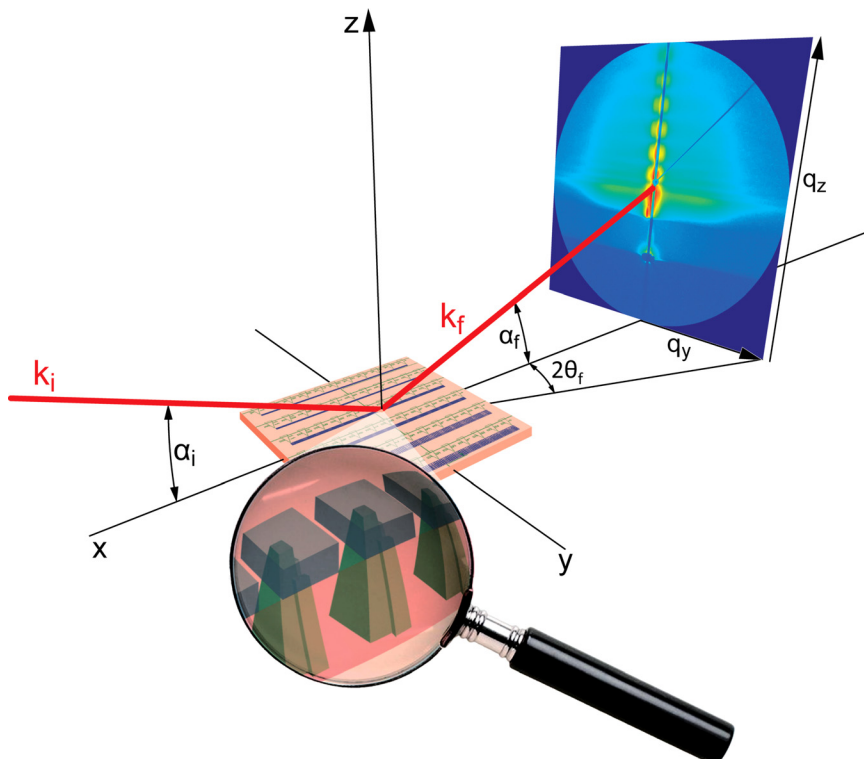

FIG. 3. Definition of angles and scattering vectors. Because of the large footprint of the X-ray beam, the sample has to be aligned perfectly parallel to it. This has been ensured by Cu structures parallel to the electrode arrays.

A Percus-Yevick model[19] in two dimensions has been applied for the interference function.

The modeling of the samples has been supported by morphological information of each layer of the samples, collected during AFM measurements. The taken images have been processed with the software *WSxM*.[20] Fig. 4(a) shows a bare substrate with a clear step structure. This step structure differs in size and shape from substrate to substrate. After deposition of the other layers, we observed a correlated roughness. The step structure was maintained. After deposition of 20 nm Fe:STO, the terraces were always maintained in their lateral dimension but their height is reduced by a factor 2. For 5 nm Ti, the structure was then maintained in both lateral and vertical dimensions. For 15 nm Ti as well as for 10 nm Al, no correlation has been observed between the structure of the Fe:STO film and the top electrodes.

Table II lists the roughness of the different layers. The RMS values are in all cases below 0.6 nm with the only exception of sample IV (10 nm Al top electrodes), which shows a significantly higher roughness of around 1.8 nm.

For the simulated GISAXS pattern, we evaluated four contributions to the overall scattering intensity, shown in Figure 5(a). This is a correlated roughness (1 and 2), a structure of supported islands (3), and the filamentary structure of oxygen vacancies inside the Fe:STO layer (4). The different types of scatterers will be discussed in the following.
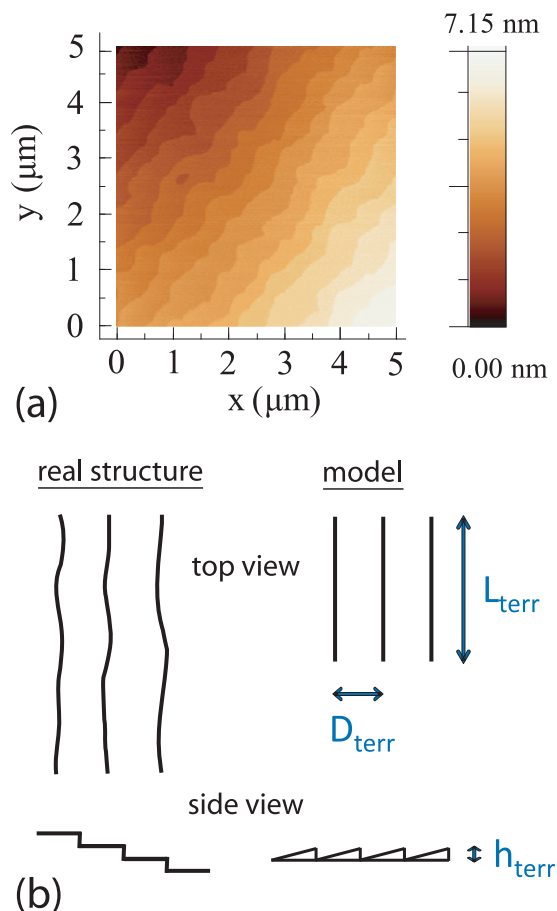
TABLE II. RMS roughness of sample layers, obtained by AFM measurements.

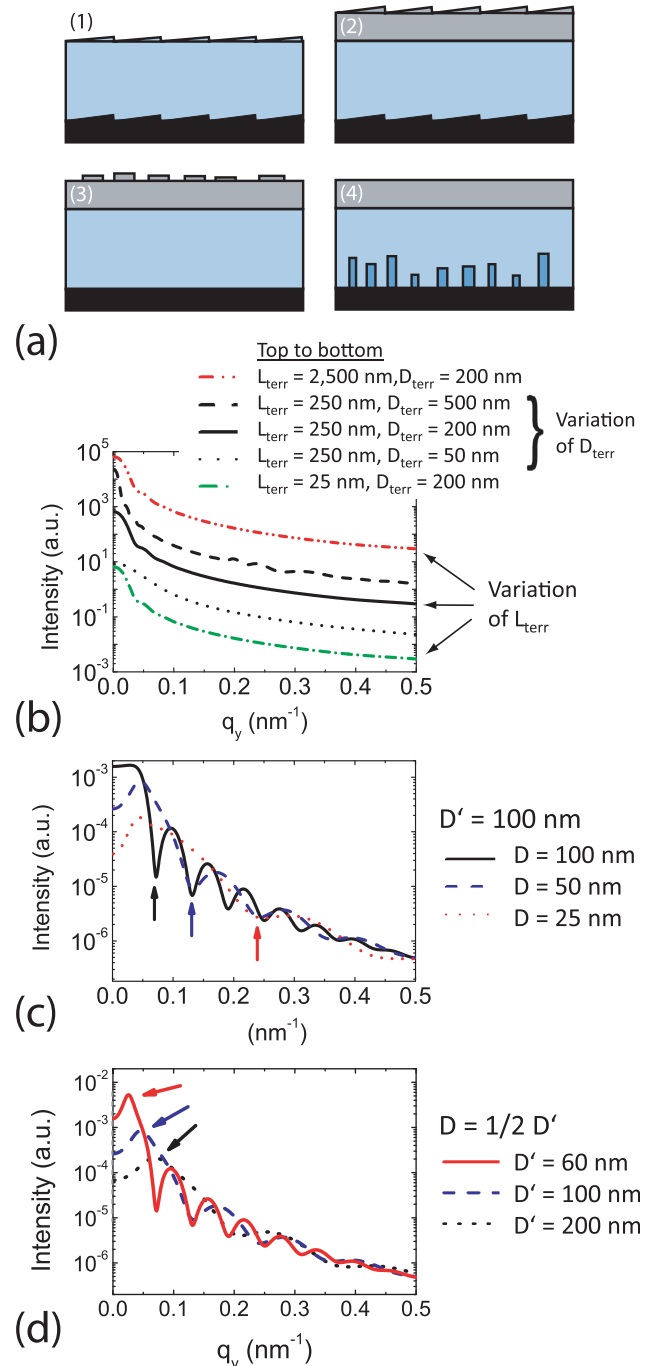|		RMS roughness
Substrate		(0.28 ± 0.13) nm
20 nm Fe:STO		(0.53 ± 0.25) nm
Top electrodes		
	20 nm Pt	(0.48 ± 0.08) nm
	5 nm Ti	(0.41 ± 0.18) nm
	10 nm Ti	(0.34 ± 0.10) nm
	15 nm Ti	(0.59 ± 0.08) nm
	10 nm Al	(1.81 ± 0.10) nm

FIG. 5. (a) The modeling of different parts of the samples which contribute to the scattering. (b) q_y-cut of intensity originating from a correlated roughness. (c) and (d) q_y-cut of intensity originating from cylindrical structures. (c) Influence of the mean diameter of cylinders. (d) Influence of the mean distance of cylinders.

FIG. 4. (a) AFM image of a bare substrate. A terrace structure can clearly be seen. (b) Modeling of the terrace structure for GISAXS simulations.

The most suitable form factor included in the simulation software to describe the terrace structure is a set of so-called "waves" that have a triangular shape, seen from the side view. Our modeling is illustrated in detail in Fig. 4(b). The terraces are described by their height h_{terr} and two variable parameters: First, their mean diameter D_{terr} perpendicular to their edge and second, a lateral correlation length L_{terr} that describes the distance for which the edge of the terraces can be approximated by being perfectly straight. During deposition of the Fe:STO layer, the step structure is maintained, leading to a correlated roughness as discussed above. The two parameters are evaluated in Fig. 5(b). The black continuous line assumes a mean diameter of the terraces of $D_{terr} = 200$ nm and a correlation length of $L_{terr} = 250$ nm. If one changes the size of the steps (D_{terr}) to 50 nm (dotted line) or to 500 nm (dashed line), a significant change in intensity can be observed: smaller steps contribute to a reduction of the undesired background. The shape of the terraces L_{terr} is evaluated as well in Fig. 5(b). It is changed to 25 nm (green line) and 2500 nm (red line). This change in intensity is much more significant compared to variations of the step size. Less straight edges of the steps reduce the background in this case. The values for both D_{terr} and L_{terr} used here were taken according to values from AFM measurements and differ in this region from substrate to substrate. For further simulations, the focus is put on the parameter L_{terr} whenever we deal with correlated roughness, since this is the parameter with the stronger influence. The correlated roughness gives a contribution to the scattering pattern from parts of the sample surface that are not covered by electrodes. This is the case for all samples. Furthermore, samples with 20 nm Pt and with 5 nm Ti show this correlation as well on the surface of their electrodes. Samples with 15 nm Ti and with 10 nm Al show only uncorrelated roughness on their electrodes.

The sputtering of Pt top electrodes leads to the growth of islands on the surface. Their mean diameter has been measured to be roughly 25 nm. For modeling this contribution, a cylindrical geometry has been used as a first approach. Samples with Al or Ti top electrodes show a much more irregular roughness. Since their morphology does not resemble a cylindrical geometry, their surface structure is incorporated with a simple roughness parameter in the simulation software.

As a first approach, conducting filaments inside the Fe:STO layer are modeled in a cylindrical geometry. One has to deal then basically with two parameters: First, their mean diameter D and second their mean distance D'.

The form factor contains information about the mean size of the scatterers. In this case, its minimum is located at $q_{y,min} = 2 \times 3.83/D$, where 3.83 is the first zero of the Bessel function. The influence of the form factor on the overall cylinder signature is evaluated in Fig. 5(c). Three values for D are plotted (100 nm: black line, 50 nm: blue line, 25 nm: red line, $D' = 100$ nm in all three cases). The dependence of the position of the first minimum as well as of the shape of the first maximum can clearly be seen.

The interference function contains information about the mean distance of the scatterers. The associated trend is shown in 5(d). The mean distance here is 200 nm (red line), 100 nm (blue line), and 60 nm (black line). A value of $D' = 1/2 D$ is assumed in the simulations.

In general, it can be stated that the mean distance of the scatterers can be found more easily in experiments than its maximum since the first maximum of the intensity is less likely covered by background scattering, originating from the sample itself.

Simulations of complete samples are shown in Fig. 6. To calculate the intensities of the different contributions to the overall scattering, the parts of the electrode arrays that are covered by top electrodes as well as the parts in between the electrodes are weighted by the area they cover. For the contribution from correlated roughness, two different lateral correlation lengths ($L_{terr} = 25$ nm (blue dashed line), 250 nm (red dashed line)) are assumed. In both cases, the diameter of the steps is $D_{terr} = 200$ nm. For the filamentary structures, different concentration of oxygen vacancies are used in the calculations in order to cover extreme cases ($SrTi_{0.99}Fe_{0.01}O_{3-x}$, $x = 0.1$ (green continuous line), 1 (orange continuous line)). This leads to a different index of refraction and therefore to a different dielectric contrast with respect to the surrounding Fe:STO matrix.

By observing the scattering intensity of the filamentary structure along the q_z-direction, a shift of its maximum, depending on the refractive index of the electrodes, has been noted (not shown here). The maximum is at $q_z = 1.69$ nm^{-1} for Pt electrodes and at $q_z = 0.80$ nm^{-1} for Ti and Al electrodes. The lateral cuts are therefore taken from vertical positions with a maximum of the filamentary structure inside the Fe:STO layer. A slight dependence of the electrode thickness is not taken into account. The scattering of three different samples has been calculated, shown in Fig. 6(a). The background is illustrated by dashed lines whereas the scattering from filaments is shown by continuous lines.

Beginning with samples with Pt top electrodes in Fig. 6(b), it can be seen that the background significantly covers the signature of the filaments inside the Fe:STO thin film. A detection of any structure inside the Fe:STO layer is not very
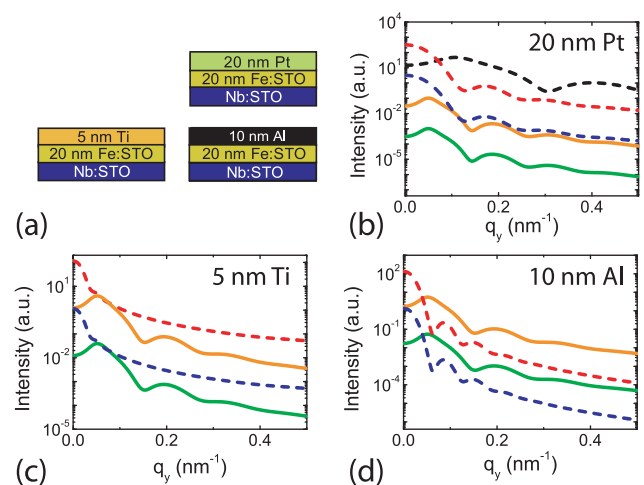

FIG. 6. (a) Sketch of the samples used for simulations. (b)–(d) Simulated q_y-cuts of intensity for the sample system: (b) 20 nm Pt/20 nm Fe:STO/Nb:STO (c) 5 nm Ti/20 nm Fe:STO/Nb:STO, and (d) 10 nm Al/20 nm Fe:STO/Nb:STO. The intensity cuts have been taken along q_z-values for which a maximum in the filament intensity was expected. Continuous lines: filament signature, (orange) $x = 1$, (green) $x = 0.1$. Dashed lines: background, (red) terraces, $L = 250$ nm, (blue) terraces, $L = 25$ nm, (black) grown islands on platinum top electrodes.

likely here. The black dashed line indicates the scattering of grown islands on top of the electrodes, which is one of the two assumed contributions to the background in this case. In later experiments, it has been found that this contribution does not dominate the overall scattering and that it is less in intensity than other parts of the background: the background itself is dominated by scattering from the correlated roughness (red and blue dashed lines) and completely covers any signal from the Fe:STO layer.

If one changes the material of the electrodes to Ti, two effects can be seen: first, the background is reduced significantly. This is also due to the fact that the correlated roughness is no longer present on top of the electrodes but only in between the electrodes. Second, the absorption of the radiation is less, leading to a higher intensity of the filamentary signature itself. The intensities are shown in Fig. 6(c). To reduce the high attenuation of the X-ray beam in the case of Pt top electrodes, one could in principle conduct experiments at higher photon energy. Nevertheless, this would not help to overcome the dominating background scattering.

In the case of Al instead of Ti (Fig. 6(d)), the background scattering is slightly higher but of the same order of magnitude in our region of interest. (The focus has to be at q_y-values where the filament signature shows its first maximum and minimum.) One reason for this could be the roughness of the Al top electrodes that distributes more strongly to out-of-plane scattering. The lower absorption of Al compared to Ti leads to a higher intensity of the filamentary signal. Considering the optimal case performed during the simulations ($L_{terr} = 25$ nm, $x = 1$), the signal to noise ratio can be increased by a factor 5×10^4 for Ti and 7×10^4 for Al if one uses the lighter elements for electrodes instead of Pt.

IV. GISAXS MEASUREMENTS

The results of the GISAXS measurements are presented in Figs. 7–10. Intensities are normalized with the integrated intensity of the incident beam and thus comparable for different measurements. For comparison, Fig. 7 shows the scattered intensity of a reference sample which consists of 20 nm Fe:STO/Nb:STO only. The same pattern is observed on the other samples if one focuses the X-ray beam next to the electrode structures. This way it can be excluded that the
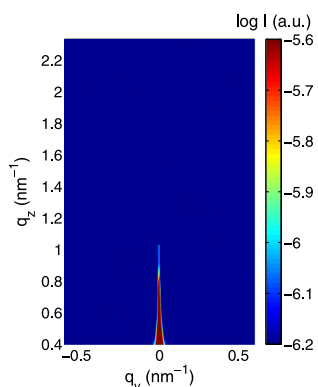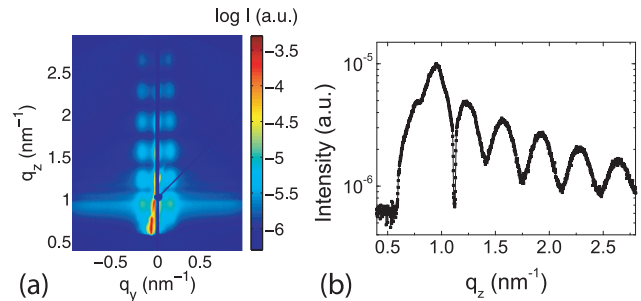

FIG. 8. GISAXS results for sample I (20 nm Pt). (a) Scattering image and (b) q_z-cut of scattering intensity along $q_y = 0.1$ nm^{-1}. The oscillations originate from the Pt layer. From their periodicity, the height of the top electrodes can be measured to be (19.8 ± 0.3) nm. In lateral cuts, no systematic change resulting from the electric treatment has been observed. This is due to the strongly scattering Pt top electrodes that cover any signal that might originate from the Fe:STO layer.

observed structures originate from changes inside the samples during the structuring process of the electrodes.

The resulting GISAXS intensity for the sample with Pt top electrodes is presented in Fig. 8(a). The scattering is dominated by the Pt top electrodes. A vertical cut (along q_z) is shown in Fig. 8(b). The oscillating intensity shows a periodicity that corresponds to (19.8 ± 0.3) nm height in real space. A similar pattern with similar periodicity was observed for a sample with 50 instead of 20 nm Fe:STO. Therefore, this oscillation is connected to the height of the Pt top electrodes. In lateral q_y-cuts at different positions, no systematic change of the intensity due to electroforming treatments has been observed. This is because of the weak intensity of filamentary structures inside the Fe:STO layer as has been shown by our simulations.

Samples II and III show a completely different GISAXS pattern in their as-deposited state (see Fig. 9(a)). A vertical cut along $q_y = 0.2$ nm^{-1} (Fig. 9(b)) shows the Yoneda peak at $q_z \approx 0.75$ nm^{-1} followed by an oscillating intensity with a periodicity of $\Delta q_z = (0.29 \pm 0.03)$ nm^{-1}, from which the height of the scatterers can be calculated to be (21.7 ± 2.2)

FIG. 7. GISAXS scattering image for a reference sample which consists of 20 nm Fe:STO/Nb:STO only.
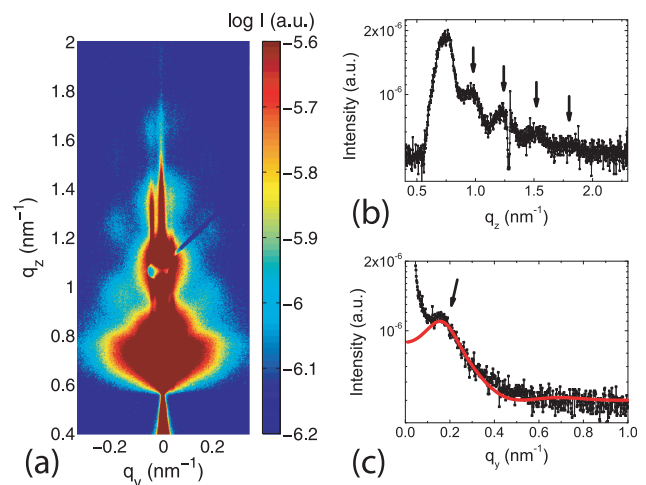

FIG. 9. GISAXS results for sample II (5 nm Ti). (a) Scattering image. A laterally formed structure can be seen. (b) Vertical cut along $q_y = 0.2$ nm^{-1}. Arrows indicate oscillations. (c) Lateral cut along $q_z = 0.95$ nm^{-1}. Red line: Simulated GISAXS intensity with an arrow indicating a maximum.
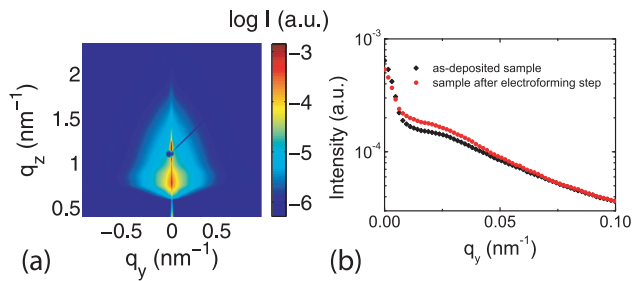
FIG. 10. GISAXS results for sample IV (10 nm Al). (a) Scattering image (b) q_y-cut along $q_z = 0.8\,\mathrm{nm}^{-1}$. Black line: as-deposited sample. Red line: sample after applying a positive voltage of a few volts. After electroforming of the sample, a significant rise of the correlation maximum in the scattering image is observed.

nm. This holds for both 5 and 15 nm Ti electrodes, and the observed structure is therefore connected to the 20 nm thick Fe:STO film. A lateral cut along $q_z = 0.95\,\mathrm{nm}^{-1}$ (Fig. 9(c)) yields a correlation maximum for the observed pattern at $q_y = 0.152\,\mathrm{nm}^{-1}$. Simulations, again with the software FitGISAXS,[18] (red line in Fig. 9(c)) have been performed to obtain more quantitative information on the scatterers, which were modeled in a first approximation as cylinders with a different electron density compared to the surrounding Fe:STO film. The simulation of the off-plane (q_y) intensity was performed in a way that the correlation maximum (arrow in Fig. 9(c)) was reproduced as well as the right slope. For this, it was assumed that the resulting pattern originates from the cylindrical structure only and thus the simulated intensity was scaled to fit with the maximum of the measured data. The cylindrical form factor then led to a minimum, which is compatible with the experimental data but masked there by noise. This minimum yields a mean cylinder diameter of $D = 15\,\mathrm{nm}$. The correlation peak gives a mean distance between the scatterers of $D' = 30\,\mathrm{nm}$. The region left to the correlation peak was not taken into account since it is dominated by in-plane scattering (cf. beam stop for the specular peak in Fig. 9(a)). It should be noted that the scattering pattern shown in Fig. 9(a) points to a filament geometry more complex than a simple cylinder. Nevertheless, the numerical values for the filament dimensions obtained in the cylinder approximation provide an estimate which compares well with AFM measurements described in Ref. 15.

The aluminium top electrodes are significantly more rough than the other surfaces prepared for our measurements. The incident intensity is thus distributed towards outside the plane of incidence, resulting in the pattern of Fig. 10(a). A lateral structure like in samples II and III (Ti top electrodes) cannot be observed. This does not necessarily mean that it is not present, since it might be covered by the stronger scattering intensity of the top electrodes. Fig. 10(b) compares the GISAXS intensity in a lateral cut along $q_z = 0.8\,\mathrm{nm}^{-1}$ in the region right next to the plane of incidence. A clear difference between the as deposited and the formed state can be observed. This effect is shown here for electrodes of $50 \times 50\,\mu\mathrm{m}^2$ size but has been observed as well systematically in the same way for the other electrode sizes. If one compares the results with our simulations, the shape of the scattered intensity in lateral (q_y) direction fits qualitatively to both the background of the terrace

structure and a filamentary structure inside the Fe:STO layer. Due to the high scattering intensity close to the plane of incidence ($q_y \approx 0$), it is difficult to obtain more detailed information from the scattering pattern. Nevertheless, if one assumes a filamentary structure inside the Fe:STO layer to cause the scattering pattern, the mean diameter of the filaments can be estimated by fitting a cylindrical form factor to reproduce the slope of the scattered intensity right next to the observed maximum. As before, the scattered intensity was scaled to fit with the measured intensity. The mean diameter of the scatterers turns out to be around 70 nm. To obtain more detailed scattering information close to the plane of incidence, GISAXS techniques with ultra small detector angles (GIUSAXS) can be used for future experiments. This way a higher resolution for smaller q_y-values can be achieved. The fact that the scattered intensity after the electrical treatment is around 13% higher than in the as-deposited state shows the general ability of GISAXS experiments to probe changes of the samples that occur due to the electrical forming step.

V. DISCUSSION AND CONCLUSION

The findings of this work are briefly summarized in Figure 11. Since Pt has a high atomic number ($Z = 78$), it is a strong scatterer and dominates the GISAXS pattern. Furthermore, due to absorption, the information depth in GISAXS experiments is too low to access the underlying Fe:STO layer. The attenuation length for Pt is only 24 nm at a photon energy of 9 keV at an angle of incidence of $0.7°$.[12] We showed that this problem can be overcome by using less scattering elements for the top electrodes. Ti ($Z = 22$) and Al ($Z = 13$) are suitable candidates for this. By performing simulations, we evaluated the dependence of different parts of the scattering pattern on geometrical dimension.

Ti and Al are both reactive elements and can cause structural changes in the active layer during electrode deposition. The reduction of the Fe:STO layer leads in the case of
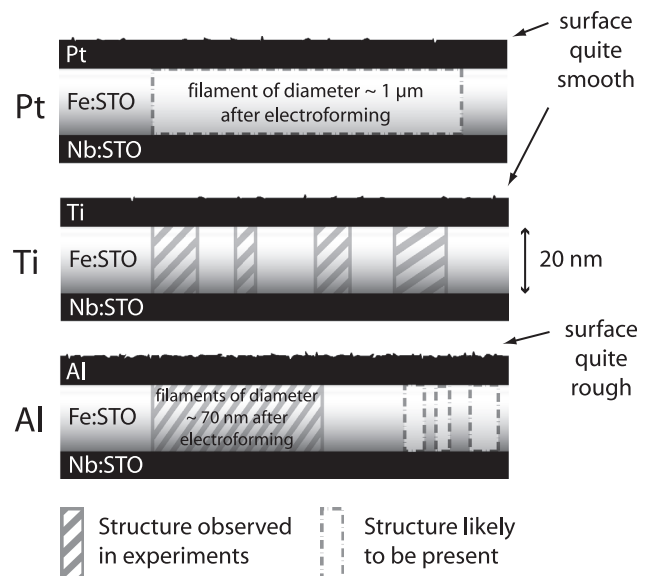

FIG. 11. Summary of results obtained during this work. Our findings clearly point at a filamentary type of the switching scenario.

Ti to the formation of conductive structures before any electrical treatment. We were able to determine their dimensions to 15 nm (mean diameter) with a mean distance of 30 nm between the scatterers. If in the case of Al, a laterally formed structure is present due to reactions with the top electrode could neither be proved nor be excluded because of the high roughness of the Al top electrodes. Nevertheless, samples with Al top electrodes not only show counter-eightwise resistive switching (that needs a first electroforming step) but also forming-free resistive switching in eightwise polarity, like it is observed with Ti top electrodes (cf. Fig. 2(c)). That is why the presence of filamentary structures is very likely in samples with Al as well.

The electrical forming step in Pt and Al samples changes significantly their electrical resistance. For Pt samples, a change in the Fe:STO layer could not be observed due to the previously explained reasons. LC-AFM measurements in Refs. 13 and 14 show the presence of a conductive structure with a diameter of around 1 μm, which is too large to be resolved in standard GISAXS measurements. By carrying out GIUSAXS experiments, structures of this size could in principle be detected, providing that the attenuation is not too high like in the case of Pt. For aluminium top electrodes, the GISAXS pattern changes due to the influence of the electroforming step, pointing at a change of the electron density distribution inside the samples. A first estimate of the dimensions of the related scatterers gives a mean diameter of around 70 nm.

In total, it can be stated that GISAXS is a useful characterization technique to gain novel insights into resistive switching in thin film devices. The results of this work explicitly prove that electroforming results in the formation of filaments rather than a homogeneous modified material beneath the electrode. Information on the mean lateral size and distance of filamentary structures, not only at the surface but also inside the whole thin film, could be obtained. Therefore, GISAXS experiments are a powerful tool to provide essential contributions to the assessment of the ultimate scaling limits of future RRAM devices.

[1] R. Waser and M. Aono, Nature Mater. **6**, 833 (2007).

[2] R. Waser, R. Dittmann, G. Staikov, and K. Szot, Adv. Mater. **21**, 2632 (2009).

[3] J. P. Strachan, M. D. Pickett, J. J. Yang, S. Aloni, A. L. D. Kilcoyne, G. Medeiros-Ribeiro, and R. S. Williams, Adv. Mater. **22**, 3573 (2010).

[4] J. P. Strachan, D. B. Strukov, J. Borghetti, J. J. Yang, G. Medeiros-Ribeiro, and R. S. Williams, Nanotechnology **22**, 254015 (2011).

[5] R. Muenstermann, T. Menke, R. Dittmann, and R. Waser, Adv. Mater. **22**, 4819 (2010).

[6] J. P. Strachan, G. Medeiros-Ribeiro, J. J. Yang, M.-X. Zhang, F. Miao, I. Goldfarb, M. Holt, V. Rose, and R. S. Williams, Appl. Phys. Lett. **98**, 242114 (2011).

[7] R. Dittmann, R. Muenstermann, I. Krug, D. Park, T. Menke, J. Mayer, A. Besmehn, F. Kronast, C. M. Schneider, and R. Waser, Proc. IEEE **100**, 1979 (2012).

[8] D.-H. Kwon, K. M. Kim, J. H. Jang, J. M. Jeon, M. H. Lee, G. H. Kim, X.-S. Li, G.-S. Park, B. Lee, S. Han, M. Kim, and C. S. Hwang, Nat. Nanotechnol. **5**, 148 (2010).

[9] F. Miao, J. P. Strachan, J. J. Yang, M.-X. Zhang, I. Goldfarb, A. C. Torrezan, P. Eschbach, R. D. Kelly, G. Medeiros-Ribeiro, and R. S. Williams, Adv. Mater. **23**, 5633 (2011).

[10] J. Levine, J. Cohen, Y. Chung, and P. Georgopoulos, J. Appl. Crystallogr. **22**, 528 (1989).

[11] G. Renaud, R. Lazzari, and F. Leroy, Surf. Sci. Rep. **64**, 255 (2009).

[12] B. Henke, E. Gullikson, and J. Davis, At. Data Nucl. Data **54**, 181 (1993).

[13] T. Menke, R. Dittmann, P. Meuffels, K. Szot, and R. Waser, J. Appl. Phys. **106**, 114507 (2009).

[14] R. Muenstermann, T. Menke, R. Dittmann, S. Mi, C.-L. Jia, D. Park, and J. Mayer, J. Appl. Phys. **108**, 124504 (2010).

[15] S. Stille, C. Lenser, R. Dittmann, A. Koehl, I. Krug, R. Muenstermann, J. Perlich, C. M. Scheider, U. Klemradt, and R. Waser, Appl. Phys. Lett. **100**, 223503 (2012).

[16] S. V. Roth, R. Doehrmann, M. Dommach, M. Kuhlmann, I. Kroeger, R. Gehrke, H. Walter, C. Schroer, B. Lengeler, and P. Mueller-Buschbaum, Rev. Sci. Instrum. **77**, 085106 (2006).

[17] A. Buffet, A. Rothkirch, R. Doehrmann, V. Koerstgen, M. M. A. Kashem, J. Perlich, G. Herzog, M. Schwartzkopf, R. Gehrke, P. Mueller-Buschbaum, and S. V. Roth, J. Synchrotron Radiat. **19**, 647 (2012).

[18] D. Babonneau, J. Appl. Crystallogr. **43**, 929 (2010).

[19] D. Kinning and E. Thomas, Macromolecules **17**, 1712 (1984).

[20] I. Horcas, R. Ferandez, J. Gomez-Rodriguez, J. Colchero, and J. Gomez-Herrero, Rev. Sci. Instrum. **78**, 013705 (2007).